INTERNATIONAL JOURNAL FOR NUMERICAL METHODS IN FLUIDS
Int. J. Numer. Meth. Fluids 2004; **45**:275–299 (DOI: 10.1002/fld.698)

Assessment of two-equation turbulence modelling for high Reynolds number hydrofoil flows

N. Mulvany[1], J. Y. Tu[1,*,†], L. Chen[2] and B. Anderson[2]

[1]*School of Aerospace, Mechanical & Manufacturing Engineering, RMIT University, P.O. Box 71, Bundoora, Vic. 3083, Australia*
[2]*Maritime Platforms Division, AMRL, Defence Science and Technology Organisation, P.O. Box 4331, Melbourne, Vic. 3001, Australia*

SUMMARY

This paper presents an evaluation of the capability of turbulence models available in the commercial CFD code FLUENT 6.0 for their application to hydrofoil turbulent boundary layer separation flow at high Reynolds numbers. Four widely applied two-equation RANS turbulence models were assessed through comparison with experimental data at Reynolds numbers of 8.284×10^6 and 1.657×10^7. They were the standard k–ε model, the realizable k–ε model, the standard k–ω model and the shear-stress-transport (SST) k–ω model. It has found that the realizable k–ε turbulence model used with enhanced wall functions and near-wall modelling techniques, consistently provides superior performance in predicting the flow characteristics around the hydrofoil. Copyright © 2004 John Wiley & Sons, Ltd.

KEY WORDS: two-equation turbulence models; hydrofoil flow; boundary layer; CFD; high Reynolds number flows

1. INTRODUCTION

Hydrodynamic flows of interest to designers of large surface and sub-surface marine vessels and their propulsors are typically characterized by high Reynolds number. Such flows can typically exceed Reynolds numbers of 10^7 [1], and can reach magnitudes of 10^{10} [2]. These flows mostly exhibit some form of unsteadiness or time-dependent phenomena, such as the shedding of vortices from propeller blades, control surfaces and other submerged appendages. Also, with the occurrence of cavitation these flows can also be multiphase. The expectations placed upon solution methodology, computational software and computer hardware to simulate

*Correspondence to: Jiyuan Tu, School of Aerospace, Mechanical and Manufacturing Engineering, RMIT University, P.O. Box 71, Bundoora, Vic. 3083, Australia.
†E-mail: Jiyuan.Tu@rmit.edu.au

Contract/grant sponsor: Maritime Platforms Division (MPD), Defence Science and Technology Organisation (DSTO)
Contract/grant sponsor: School of Aerospace, Mechanical and Manufacturing Engineering, RMIT University

Received 2 September 2003
Revised 5 January 2004

these hydrodynamic flows are immense. Although the emergence of parallel computing and its provision of reduced global memory and run-times through multiple processors, analysis of such complex flows by direct numerical simulation (DNS) is still untenable and although, the alternative technique, large-Eddy simulation (LES), is improving, it remains practically expensive. The modelling of high Reynolds number flows continues to be based on the solution of the Reynolds-averaged Navier–Stokes (RANS) equations. It is the latter methodology that allows numerical solutions to be determined for those complex problems [3]. Parts of a larger three-dimensional flow problems that were previously simulated individually are now being simulated as complete configurations, such as full submarine geometries comprising hull, sail, stern appendage, propeller and moving control surfaces for both steady and unsteady flow scenarios [3]. This also has to be attributed to the development of advanced turbulence models, such as the widely adopted two-equation turbulence models.

Although such complex problems can be computationally handled with the help of advanced turbulence models, there are questions whether the available turbulence models are predicting the correct flow physics, and which turbulence models are best suited to what type of flows. Arashahi [3] suggests that it is naive to assume the validity of a turbulence model over a wide range of flows, and that unique modification or refinement of existing turbulence models for specific flow applications may provide improved performance. Many evaluations of two-equation RANS turbulence models documented in the literature have been undertaken in order to identify the most suitable model for the particular flow of interest.

Speziale *et al.* [4] applied a variety of two-equation (k–ε and k–ω variants) models and their k–τ model to near-wall turbulent flows. They concluded that due to the excessively high levels of destruction–dissipation and turbulence viscosity near the wall, the predictions of the tested k–ε models were severely compromised. The k–ω model of Wilcox *et al.* [5, 6] had the same constraints as the k–ε models, yet returned excessive turbulent kinetic energy near the wall. However, for many applications, the k–ω model provided adequate prediction of the skin friction at the wall and the turbulence statistics away from the wall. Based on the numerical tests of Speziale *et al.* [4], the k–τ turbulence model showed improved predictions within the turbulent boundary layer.

Lien and Leschziner [7] examined a non-linear eddy-viscosity model and a second-moment closure model by applying them to 2D separated flow from a high-lift airfoil. They concluded that the second-moment closure produced superior predictions relative to both the non-linear eddy-viscosity model and the realizable Reynolds stress algebraic model of Shih *et al.* [8]. The second-moment closure model had the inherent ability of representing the interaction between streamline curvature and turbulence anisotropy, and the effect of anisotropy on shear stress. Nevertheless, the second-moment model failed to predict the onset of separation at the correct angle of attack. The failure was attributed to the excessively high levels of shear stress near the wall, preventing separation.

Pajayakrit and Kind [9] evaluated four turbulence models for predicting the development of plane and curved wall jet flows. The models evaluated were the Baldwin and Lomax [10] algebraic model, the Dash *et al.* [11] k–ε model, the Wilcox [5] k–ω and the Wilcox [6] multi-scale model. Without any modification, all models demonstrated significant deficiencies, although the Dash *et al.* [11] k–ε model performed reasonably well in an overall sense, particularly for the curved wall jet flow. Fine tuning of the Wilcox [5, 6] models was undertaken by adjusting the model constants, however, improvement was achieved by the modified k–ω model only.

The work presented by Speziale *et al.* [4], Lien and Leschziner [7] and Pajayakrit and Kind [9] is essential for the continued development of turbulence models, but it does not fully specify which turbulence models should be used. The analysis of the turbulence models in these references is usually performed at a complex level, a level beyond most users, and typically the models are evaluated using fundamental fluid mechanics problems, not more useful practical problems.

Unlike the work presented by Speziale *et al.* [4], Lien and Leschziner [7] and Pajayakrit and Kind [9], Kim *et al.* [12] evaluated three widely applied and economic turbulence models for a practical problem; the hull form design of a very large crude-oil carrier. The turbulence models evaluated were the standard k–ε model, the RNG k–ε model and the realizable k–ε model. Emphasis was placed on their ability to accurately predict the nominal wake distribution at the propeller plane, a region of strong bilge vortices and complex flow behaviour, as flow information within this region is vital for propeller design. It was determined that the realizable k–ε turbulence model accurately predicted the strength and location of the bilge vortex, but both the standard k–ε and RNG k–ε turbulence models failed to predict this flow feature. All three turbulence models predicted differences for the two hull forms with respect to wake distribution and pressure drag, but again the standard k–ε and RNG k–ε turbulence models showed poorer correlation to the experimental data [12].

This paper is not intended as an authoritative reference for turbulence model applications for all hydrodynamic flow simulations, nor do we aim to discuss the strengths and weaknesses of the turbulence models at a complex level. Rather, like the work presented by Kim *et al.* [12], it is intended as a guide to researchers and designers who are working on a similar problem: hydrofoil flow at high Reynolds number. The characteristics of this flow are that the boundary layer on the suction surface is subjected to a large adverse pressure gradient, where the boundary layer separation commences. This category of turbulent flow poses major modelling challenges on the predictive capabilities of any turbulence model.

Such turbulent boundary layer separation occurs at the trailing edge of hydrofoils operating at high Reynolds numbers, resulting in the formation of unsteady oscillating wakes. Under certain conditions, the vortex-shedding period of the wake may become coincident with the resonant frequency of the hydrofoil or parts of it, resulting in the emission of a tonal noise. Such an emission from lifting surfaces associated with naval vessels is highly undesirable, as this noise is a dominant source of information for underwater detection systems.

This preliminary study investigates several two-equation RANS turbulence models included in the commercial CFD code FLUENT 6.0 [13], and evaluates their ability to model turbulence associated with such flows. The four turbulence models evaluated are the standard k–ε, the realizable k–ε, the standard k–ω and the relatively new shear-stress transport (SST) k–ω. Also, in an effort to provide researchers with a guide to the application of wall functions in such a flow scenario, three different wall treatments are investigated with respect to their suitability. These include two different wall functions, the standard and non-equilibrium variants, and an enhanced wall treatment employing near-wall modelling techniques. The developed CFD model is based on the characteristics and parameters of the recent experimental research into high-Reynolds number hydrofoil flow, undertaken by Bourgoyne *et al.* [1, 14, 15], allowing direct comparison with high-quality experimental data.

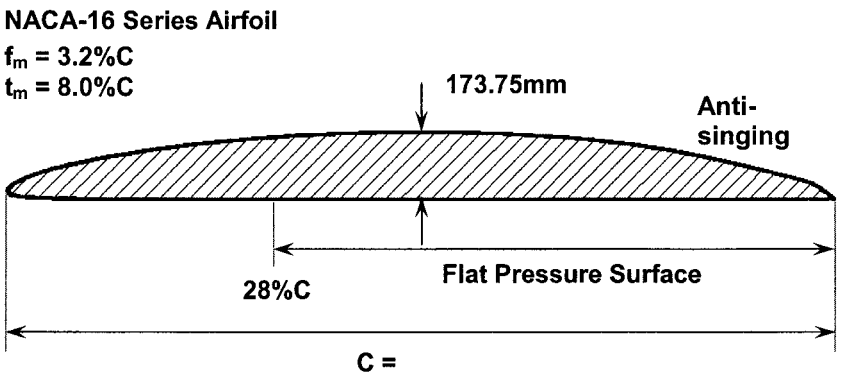

Figure 1. The two-dimensional hydrofoil geometry as used by Bourgoyne *et al.* [1, 14, 15] (Adapted from 1).

2. PROBLEM OVERVIEW

The main objective of the experimental research conducted by Bourgoyne *et al.* [1, 14, 15] was to identify and document the dominant flow features in the trailing edge region of a hydrofoil operating at chord-based Reynolds numbers approaching 10^8. The research was conducted in the William B. Morgan Large Cavitation Channel (LCC) in Memphis, TN. The test hydrofoil was fully two-dimensional, spanning the test section (3.05 m), with a chord length (C) of 2.134 m. The cross-section profile was representative of a generic naval propeller of moderate thickness (t) and camber (f), utilising an NACA-16 airfoil profile ($t/C = 0.08$, $f/C = 0.032$) with two modifications. A detailed diagram of the hydrofoil geometry is illustrated in Figure 1 and the anti-singing trailing edge geometry is well detailed in Bourgoyne *et al.* [1].

Although the application of numerical methods to hydrodynamic lifting-surface flow is widespread in References [16–19] and has greatly matured, there are specific challenges posed to numerically modelling the experimental tests conducted by Bourgoyne *et al.* [1, 14, 15]. Firstly, the experimental testing was conducted at such high Reynolds numbers that the validity and confidence of the turbulence models required by the numerical model may be degraded. Of particular importance to this preliminary steady-state analysis is boundary layer separation. In this flow, configuration with a slender and streamlined body, the numerical modelling of turbulent boundary layer separation is more challenging due to its Reynolds number dependency. It has been shown experimentally by both Baubeau and Latorre [17] and Bourgoyne *et al.* [1] that at a constant angle of attack, a turbulent boundary layer resists separation further along the surface of a hydrofoil, separating closer to the trailing edge with increasing Reynolds number.

3. THEORY

The governing equations for the turbulent incompressible flow encountered in this research are the steady-state RANS equations for the conservation of mass and momentum, which are presented in the following forms [13]:

Continuity:

$$\frac{\partial}{\partial x_i}(\rho \bar{u}_i) = 0 \tag{1}$$

Momentum:

$$\frac{\partial}{\partial x_j}(\rho \bar{u}_i \bar{u}_j) = -\frac{\partial \bar{p}}{\partial x_i} + \frac{\partial}{\partial x_j}\left[\mu\left(\frac{\partial \bar{u}_i}{\partial x_j} + \frac{\partial \bar{u}_j}{\partial x_i} - \frac{2}{3}\delta_{ij}\frac{\partial \bar{u}_l}{\partial x_l}\right)\right] + \frac{\partial}{\partial x_j}(-\rho\overline{u_i' u_j'}) \tag{2}$$

Here, $\bar{\rho}$ is averaged density, $\bar{p}$ is averaged pressure, μ is the molecular viscosity and $-\rho\overline{u_i' u_j'}$ is the Reynolds stress. To correctly account for turbulence, Reynolds stresses are modelled in order to achieve closure of Equation (2). The method of modelling employed utilizes the Boussinesq hypothesis to relate the Reynolds stresses to the mean velocity gradients within the flow. Therefore, the Reynolds stresses are given by

$$-\rho\overline{u_i' u_j'} = \mu_t\left(\frac{\partial \bar{u}_i}{\partial x_j} + \frac{\partial \bar{u}_j}{\partial x_i}\right) - \frac{2}{3}\left(\rho k + \mu_t \frac{\partial \bar{u}_i}{\partial x_i}\right)\delta_{ij} \tag{3}$$

where μ_t is the turbulent (or eddy) viscosity and k is the turbulent kinetic energy. For two-equation turbulence models such as the k–ε and k–ω variants, the turbulent viscosity is computed through the solution of two additional transport equations for the turbulent kinetic energy, and either the turbulence dissipation rate, ε, or the specific dissipation rate, ω.

3.1. Transport equations of turbulent quantities

The transport equation for the turbulent quantity $\phi - k$, ε and ω-is given by

$$\frac{\partial}{\partial x_i}(\rho \phi \bar{u}_i) = \frac{\partial}{\partial x_j}\left[\left(\mu + \frac{\mu_t}{\sigma_\phi}\right)\frac{\partial \phi}{\partial x_j}\right] + G_\phi - Y_\phi \tag{4}$$

The transport equation for k is physically correct, however the transport equation for both ε and ω are heavily modelled [13]. For different two-equation turbulence models, the turbulent Prandtl number σ, production term, G_ϕ and dissipation term, Y_ϕ, will be modelled differently.

3.1.1. Standard k–ε turbulence model. In standard, the production term is given by

$$G_k = \mu_t S^2 \tag{5}$$

where, S is the modulus of the mean rate-of-strain tensor, defined by

$$S \equiv \sqrt{2 S_{ij} S_{ij}}, \quad S_{ij} = \frac{1}{2}\left(\frac{\partial \bar{u}_j}{\partial x_i} + \frac{\partial \bar{u}_i}{\partial x_j}\right)$$

The dissipation of this turbulence kinetic energy, Y_k, is defined by

$$Y_k = \rho \varepsilon \tag{6}$$

The production and dissipation of ε, G_ε and Y_ε, respectively, are defined as

$$G_\varepsilon = C_{1\varepsilon} \frac{\varepsilon}{k} (G_k) \tag{7}$$

$$Y_\varepsilon = C_{2\varepsilon} \rho \frac{\varepsilon^2}{k} \tag{8}$$

The turbulent viscosity is thus calculated by

$$\mu_t = \rho C_\mu \frac{k^2}{\varepsilon} \tag{9}$$

The model constants applied in the standard k–ε turbulence model are given by

$$C_{1\varepsilon} = 1.44, \quad C_{2\varepsilon} = 1.92, \quad C_\mu = 0.09, \quad \sigma_k = 1.0, \quad \sigma_\varepsilon = 1.3$$

3.1.2. Realizable k–ε turbulence model. In the realizable k–ε turbulence model, the production and dissipation terms are defined as

$$G_\varepsilon = \rho C_1 S \varepsilon \tag{10}$$

$$Y_\varepsilon = \rho C_2 \frac{\varepsilon^2}{k + \sqrt{v\varepsilon}} \tag{11}$$

In Equations (10) and (11), C_2 is a constant, while C_1 is defined as

$$\begin{aligned} C_1 &= \max\left[0.43, \frac{\eta}{\eta + 5}\right] \\ \eta &= S \frac{k}{\varepsilon} \end{aligned} \tag{12}$$

Similarly to the standard k–ε turbulence model, the turbulent viscosity is computed using Equation (9), however, C_μ is no longer a constant. C_μ is calculated using the following equations:

$$C_\mu = \frac{1}{A_0 + A_s(kU^*/\varepsilon)} \tag{13}$$

where

$$U^* \equiv \sqrt{S_{ij}S_{ij} + \tilde{\Omega}_{ij}\tilde{\Omega}_{ij}}$$

$$\tilde{\Omega}_{ij} = \Omega_{ij} - 2\varepsilon_{ijk}\omega_k, \quad \Omega_{ij} = \frac{1}{2}\left(\frac{\partial \bar{u}_i}{\partial x_j} - \frac{\partial \bar{u}_j}{\partial x_i}\right)$$

In Equation (13), A_0 is a constant and the remaining variable, A_s, is calculated using the following:

$$A_s = \sqrt{6}\cos\phi$$

where

$$\phi = \frac{1}{3}\cos^{-1}(\sqrt{6}W), \quad W = \frac{S_{ij}S_{jk}S_{ki}}{\tilde{S}^3}, \quad \tilde{S} = \sqrt{S_{ij}S_{ij}}$$

The constants applied in the realizable k–ε turbulence model are equal to

$$\sigma_k = 1.0, \quad \sigma_\varepsilon = 1.2, \quad C_2 = 1.9, \quad A_0 = 4.04$$

3.1.3. Standard k–ω turbulence model. The modelled transport equation for k in the standard k–ω turbulence model is very similar to that of the k–ε-based models. The production of turbulence kinetic energy is defined identically to that of the k–ε models (Equation (5); however, the standard k–ω model has a different formulation for the diffusion of k, defined as

$$Y_k = \rho\beta^*_\infty f_{\beta^*} k\omega \tag{14}$$

where β^*_∞ is a constant and

$$f_{\beta^*} = \begin{cases} 1, & \chi_k \leqslant 0 \\ \left[\dfrac{1+680\chi_k^2}{1+400\chi_k^2}\right], & \chi_k > 0 \end{cases} \qquad \chi_k \equiv \frac{1}{\omega^3}\frac{\partial k}{\partial x_j}\frac{\partial \omega}{\partial x_j}$$

The production and diffusion terms of ω are significantly different to those of ε. The production and dissipation of ω in the high-Reynolds number form of the standard k–ω model are defined, respectively, as

$$G_\omega = \frac{\omega}{k} G_k \tag{15}$$

$$Y_\omega = \rho\beta_i f_\beta \omega^2 \tag{16}$$

where β_i is a constant and

$$f_\beta = \frac{1+70\chi_\omega}{1+80\chi_\omega}, \quad \chi_\omega = \left|\frac{\Omega_{ij}\Omega_{jk}S_{ij}}{(\beta^*_\infty\omega)^3}\right|$$

Again, another deviation of the standard k–ω from the previous turbulence models is the computation of the turbulent viscosity. For the high Reynolds number form of the standard k–ω model, the turbulent viscosity is calculated using

$$\mu_t = \frac{\rho k}{\omega} \tag{17}$$

The constants applied in the high Reynolds number form of the standard k–ω turbulence model are equal to

$$\sigma_k = 2.0, \quad \sigma_\omega = 2.0, \quad \beta^*_\infty = 0.09, \quad \beta_i = 0.072$$

3.1.4. SST k–ω. In the SST k–ω turbulence model, the modelled transport equation for k is identical to that of the standard k–ω model; however, the transport equation for ω differs slightly with the inclusion of a cross-diffusion term, D_ω.

The production of k in the SST k–ω model is defined in the same manner as per the standard k–ω model; hence, the k–ε-type models, by Equation (5). However, variations exist in the production of ω with comparison to the standard k–ω model. The production of ω is given by

$$G_\omega = \frac{\alpha_\infty}{\nu_t} G_k \tag{18}$$

where

$$\alpha_\infty = F_1 \alpha_{\infty,1} + (1 - F_1)\alpha_{\infty,2}, \quad \alpha_{\infty,1} = \frac{\beta_{i,1}}{\beta^*_\infty} - \frac{\kappa^2}{\sigma_{\omega,1}\sqrt{\beta^*_\infty}}, \quad \alpha_{\infty,2} = \frac{\beta_{i,2}}{\beta^*_\infty} - \frac{\kappa^2}{\sigma_{\omega,2}\sqrt{\beta^*_\infty}}$$

The dissipation of the k and ω are defined differently to the standard k–ω model by the following, respectively:

$$Y_k = \rho \beta^* k \omega \tag{19}$$

$$Y_\omega = \rho \beta_i \omega^2 \tag{20}$$

where

$$\beta_i = F_1 \beta_{i,1} + (1 - F_1)\beta_{i,2} \tag{21}$$

In Equation (21), $\beta_{i,1}$ and $\beta_{i,2}$ are constants while the F_1 is determined from the following:

$$F_1 = \tanh(\Phi_1^4)$$

$$\Phi_1 = \min\left[\max\left(\frac{\sqrt{k}}{0.09\omega y}, \frac{500\mu}{\rho y^2 \omega}\right), \frac{4\rho k}{\sigma_{\omega,2} D^+_\omega y^2}\right],$$

$$D^+_\omega = \max\left[2\rho \frac{1}{\sigma_{\omega,2}} \frac{1}{\omega} \frac{\partial k}{\partial x_j} \frac{\partial \omega}{\partial x_j}, 10^{-20}\right]$$

In the previous equations, y is the distance to the next surface and D^+_ω is the positive portion of the cross-diffusion term (to be introduced at a later stage).

Unlike the standard k–ω model where the turbulent Prandtl numbers for k and ω (σ_k and σ_ω) are constants, in the SST k–ω model they are defined by

$$\sigma_k = \frac{1}{F_1/\sigma_{k,1} + (1 - F_1)/\sigma_{k,2}} \tag{22}$$

$$\sigma_\omega = \frac{1}{F_1/\sigma_{\omega,1} + (1 - F_1)/\sigma_{\omega,2}} \tag{23}$$

Returning to the cross-diffusion term, as the SST k–ω model is based upon both the standard k–ω and the standard k–ε model, the k–ε model has been transformed into equations based on k and ω, hence the cross-diffusion term, D_ω. This term is defined as

$$D_\omega = 2(1 - F_1)\rho\sigma_{\omega,2}\frac{1}{\omega}\frac{\partial k}{\partial x_j}\frac{\partial \omega}{\partial x_j} \tag{24}$$

Unlike the standard k–ω model, however, the turbulent viscosity formulation is given for the high-Reynolds number form of the SST k–ω models as

$$\mu_t = \frac{\rho k}{\omega}\frac{1}{\max[1, \Omega F_2/a_1\omega]} \tag{25}$$

where

$$\Omega \equiv \sqrt{2\Omega_{ij}\Omega_{ij}}, \quad F_2 = \tanh(\Phi_2^2), \quad \Phi_2 = \max\left[2\frac{\sqrt{k}}{0.09\omega y}, \frac{500\mu}{\rho y^2 \omega}\right]$$

The constants applied in the high Reynolds number form of the SST k–ω turbulence model are equal to

$$\sigma_{k,1} = 1.176, \quad \sigma_{\omega,1} = 2.0, \quad \sigma_{k,2} = 1.0,$$
$$\sigma_{\omega,2} = 1.168, \quad \alpha_1 = 0.31, \quad \beta_{i,1} = 0.075,$$
$$\beta_{i,2} = 0.0828, \quad \kappa = 0.41$$

4. NUMERICAL METHODS

4.1. Computational domain and mesh

The computational domain extended 1.5 C upstream of the leading edge of the hydrofoil, 1.5 C above and below the pressure surface and 3 C downstream from the trailing edge. Velocity inlet boundary conditions were applied upstream, above and below the hydrofoil, while downstream an outflow boundary condition was used. The pressure and suction surfaces of the hydrofoil were defined independently with no-slip wall boundary conditions.

The selection of the boundary conditions and dimensions of the computational domain were an approximation to the free field, not the water tunnel's test section used in Reference [1]. However, the effect of the wall of the tunnel was considered based on the method adopted in Reference [15].

A finite volume method was employed to obtain a solution of the spatially averaged Navier–Stokes equations. The coupling between the pressure and velocity fields was achieved using the SIMPLE technique. A second-order upwind scheme was used for the convection and the central-differencing scheme for diffusion terms.

An unstructured mesh arrangement with quadrilateral elements was adopted to map the flow domain (Figure 2). Particular attention was directed to an offset 'inner region' encompassing

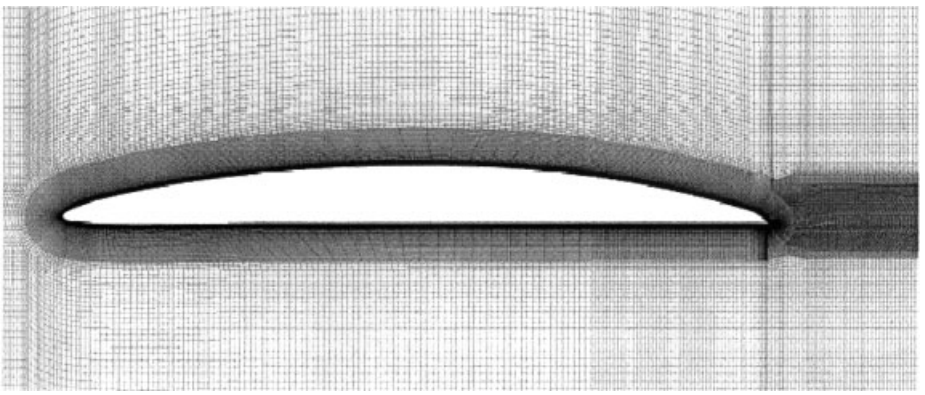

Figure 2. Computational grids around the foil.

the hydrofoil. Within this region a fine O-type mesh was applied to achieve sufficient resolution of the hydrofoil surface and the boundary layer region. Continuing downstream from the trailing edge of the inner region was the 'wake region'. A fine H-type mesh was applied within this region to accurately resolve the near and far-wake flow behaviour. The remaining 'outer region' of the domain was discretized with a much coarser H-type mesh. The mesh around the foil is shown in Figure 2.

It should be noted that on the experimental hydrofoil used by Bourgoyne *et al.* [1, 14, 15], the trailing edge was ground to a 0.397 mm radius, however, to allow improved surface discretization and mesh quality at the trailing edge of the numerical model this radius was increased to 1.5 mm.

The experimental hydrofoil was CNC machined from a solid casting of Ni–Al Bronze. The RMS surface roughness height, after polishing, was determined to be 2.5×10^{-7} m [14]. It was assumed that the roughness distribution was 'uniform sand-grain', allowing the use of a roughness constant of 0.5. Information on the flow condition within the LCC's test section during the experimental testing was not explicitly detailed by Bourgoyne *et al.* [1, 14, 15], only that it was 'a low turbulence water tunnel' [15]. The LCC's 'low turbulence' intensity was on the order of 0.1% according to Reference [20]. This value was assessed as reasonable and applied to all applicable boundary conditions.

4.2. Wall functions

The application of wall functions to model the near-wall region may significantly reduce both the processing and storage requirements of a numerical model, while producing an acceptable degree of accuracy. The principal of the wall function is to 'bridge' the viscous flow near a wall and link the solution variables at the wall-adjacent cells to the corresponding quantities at the wall.

Three wall treatments—standard wall function, non-equilibrium wall function and enhanced wall treatment [13], were investigated. For the standard wall function, a logarithmic law of the wall for mean velocity is applied. In non-equilibrium wall function, the law-of-the-wall for mean velocity is sensitized to pressure gradient effects and a two-layer-based concept is applied to calculate the cell-averaged turbulence kinetic energy production and dissipation

in wall-adjacent cells. The enhanced wall treatment is a method of near-wall modelling that utilizes the combination of a two-layer zonal model with enhanced wall functions.

5. RESULTS AND DISCUSSION

5.1. Grid independence analysis

A grid independence analysis was conducted using four meshes of varying cell number. Each mesh was processed using the realizable k–ε turbulence model with enhanced wall treatment, at a free-stream velocity of 3 m/s ($Re = 8.284 \times 10^6$). Table I details the node and y^+ characteristics of each mesh, highlighting the refinements between the subsequent meshes *A*, *B*, *C* and *D*.

Both meshes *C* and *D* achieve considerably low average y^+ values, sufficiently resolving the laminar sub-layer (i.e. $y^+ \leqslant 4$–5). Although having a minimum y^+ value well within the laminar sub-layer, the maximum and average values of mesh *B* indicate that its resolution extends to the buffer layer only (i.e. $5 \leqslant y^+ \leqslant 30$). Also, with a sufficiently low minimum y^+, mesh *A* shows significant coarseness with considerably larger maximum and average y^+ values, indicating resolution to the turbulent outer layer only (i.e. $y^+ \geqslant 30$).

Table II shows the predicted pressure-derived lift and drag coefficients, with the use of meshes *C* and *D* predicting almost identical coefficients, suggesting that the solution has converged and grid independence has been achieved.

Figure 3 displays the pressure surface boundary layer normalized mean velocity profiles at 93%C, predicted using each mesh. The velocity profiles predicted using meshes *C* and *D* are

Table I. Grid independence analysis—mesh node and y^+ characteristics.

	Nodes	Surface nodes	Maximum Y^+	Minimum y^+	Average y^+
Mesh A	42 282	570	220.11	3.37	104.35
Mesh B	98 704	1060	31.05	0.44	14.30
Mesh C	208 416	1590	4.06	0.09	2.31
Mesh D	244 026	1590	1.22	0.01	0.68

Table II. Grid independence analysis—pressure-derived lift and drag coefficients.

	Lift coefficient		Drag coefficient	
	0.5520		0.0027	
Experimental	Predicted	Error (%)	Predicted	Error (%)
Mesh A	0.4945	10.42	0.0029	7.41
Mesh B	0.5230	5.25	0.0025	7.41
Mesh C	0.5302	3.95	0.0024	11.11
Mesh D	0.5305	3.89	0.0024	11.11

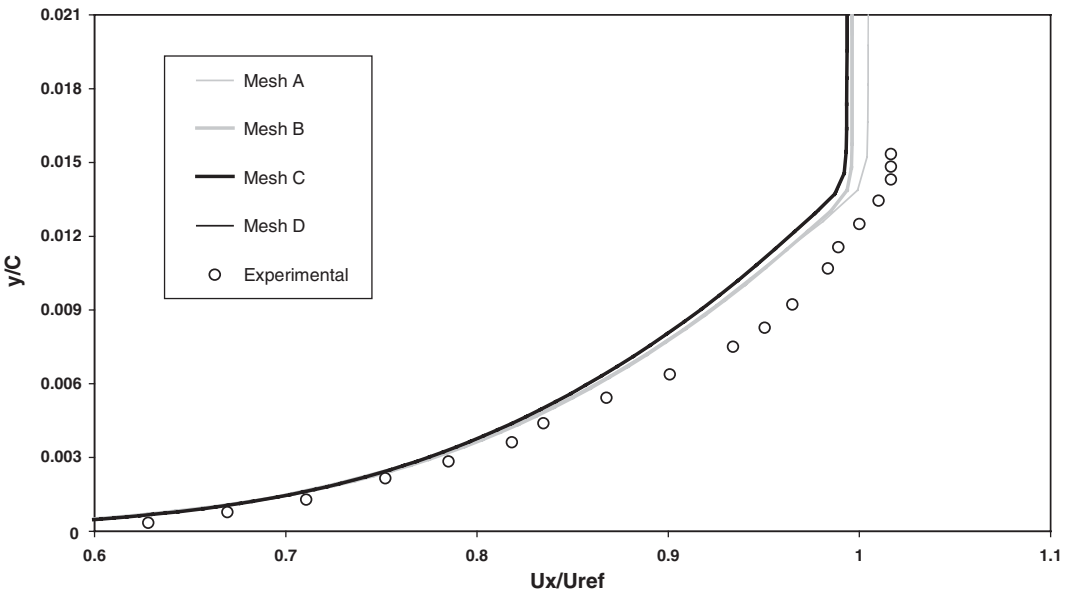

Figure 3. Grid independence analysis: pressure surface boundary layer normalized streamwise mean velocity profile at 93%C ($U_\infty = 3$ m/s).

identical and show clear differences from those of meshes *A* and *B*, again suggesting grid independence with the two finest meshes.

Therefore, with mesh *C* and mesh *D* predicting almost identical results, it is concluded that a suitable degree of grid independence is shown by the numerical solution. In consideration of the processing infrastructure and time constraints, it was concluded that the marginal performance advantages provided by the finest mesh (mesh *D*) did not justify the increased cell numbers ($\approx 16\%$) and extended CPU processing times. Henceforth, all numerical solutions discussed were obtained using mesh *C*.

5.2. *Turbulence model performance*

The results of the performance of each turbulence model presented are with respect to the predicted pressure coefficient distribution, the pressure surface boundary layer, suction surface boundary layer separation and the trailing edge and far-wake flow. The performance of each turbulence model is assessed at chord-based Reynolds numbers of 8.284×10^6 ($U_\infty = 3$ m/s) and 1.657×10^7 ($U_\infty = 6$ m/s).

All presented data are dimensionless: co-ordinate locations are referenced to the chord length (i.e. x/C and y/C) and all mean velocities are normalized with the free-stream velocity. The computed results are corrected based on the method detailed in Reference [1] to account for the effect of the walls of the test section.

The pressure coefficient distribution at the surface of the hydrofoil as predicted by each turbulence model, at a free-stream velocity of 3 m/s is illustrated in Figure 4 (A negative scale is used to assist comparison with the physical surfaces of the hydrofoil). The pressure

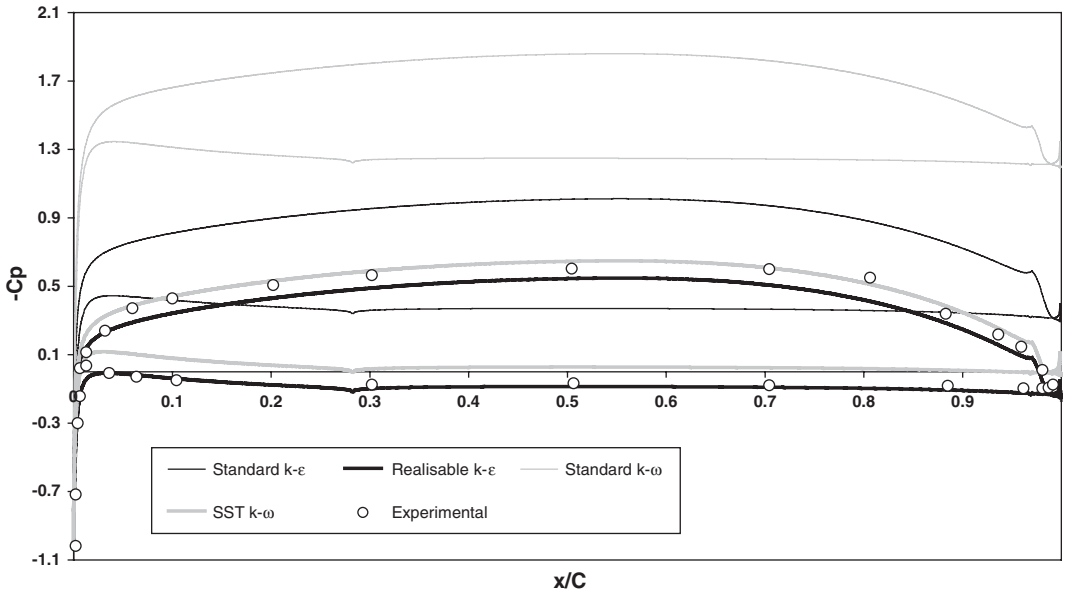

Figure 4. Turbulence model performance: pressure coefficient (C_P) distribution at the surface of the hydrofoil ($U_\infty = 3\,\mathrm{m/s}$).

distributions predicted by all models show a significant deviation from the experimental data at the suction surface, and both standard k–ε and standard k–ω were also over-predicting pressure at the front stagnation point. It seems that the realizable k–ε model provides a better prediction at the front of the hydrofoil, while the SST k–ω works better at the rear region of the foil. Nevertheless, the pressure-based lift coefficient predicted by the models for 3 m/s were 0.5113–0.5447. They were in an excellent agreement with the experimental data (0.552), given that the experimental uncertainty was 16%.

5.2.1. Pressure surface boundary layer. Figures 5 and 6 illustrate the numerical and experimental pressure surface boundary layer velocity profiles at 93%C (inverted for clarity), at a free-stream velocity of 3 and 6 m/s, respectively. As the pressure surface is largely flat beyond 28%C with only moderate surface gradients prior to this point, it can be approximated as a flat plate. Therefore, also shown in those figures is the theoretically predicted turbulent boundary layer velocity profile, calculated using classical turbulent boundary layer equations [21]. Each turbulence model predicts a differing velocity profile with varying degrees of correlation to the experimental data. A poor correlation is expected by the theoretical velocity profile.

It can be seen that the standard k–ε, standard k–ω and SST k–ω turbulence models all over-predict a boundary layer thickness compared with the experimental result. The discrepancy between the prediction and experimental data is due to the over-predicted turbulent viscosity. The turbulence model that most accurately predicts the boundary layer velocity profile is the realizable k–ε model. Close to the surface (i.e. $y/C < 0.005$) this model predicts the boundary layer characteristics exceptionally well and continues to maintain a high degree of correlation

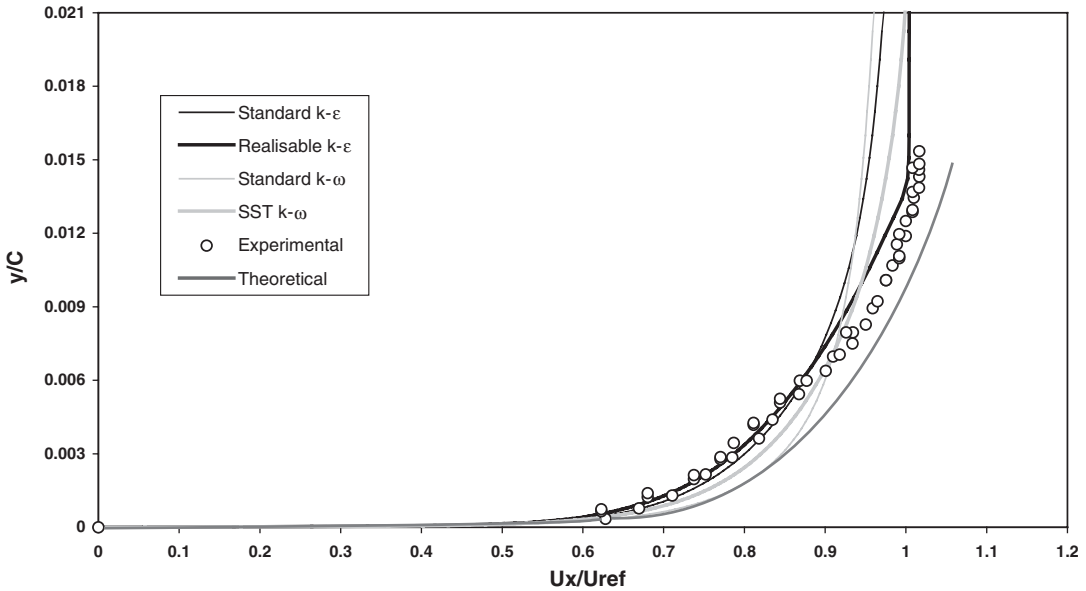

Figure 5. Turbulence model performance: pressure surface boundary layer normalized mean velocity profile at 93%C ($U_\infty = 3$ m/s).

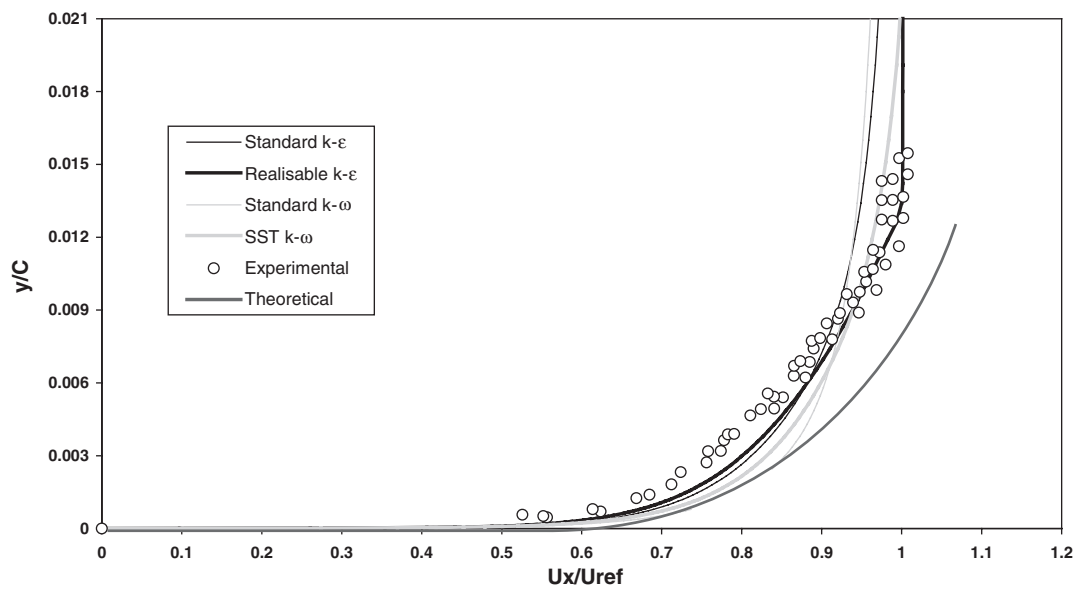

Figure 6. Turbulence model performance: pressure surface boundary layer normalized mean velocity profile at 93%C ($U_\infty = 6$ m/s).

Table III. Turbulence model performance: pressure surface boundary layer parameters at 93%C ($U_\infty = 3$ m/s).

			Numerical			
Parameter	Exp. (mm)	Theo. (mm)	Standard k–ε (mm)	Realizable k–ε (mm)	Standard k–ω (mm)	SST k–ω (mm)
Thickness (δ)	29.62	30.73	78.27	27.79	115.82	37.82
Displacement thickness (δ^*)	4.27	3.85	4.99	3.86	4.94	3.58

Table IV. Turbulence model performance: pressure surface boundary layer parameters at 93%C ($U_\infty = 6$ m/s).

			Numerical			
Parameter	Exp. (mm)	Theo. (mm)	Standard k–ε (mm)	Realizable k–ε (mm)	Standard k–ω (mm)	SST k–ω (mm)
Thickness (δ)	27.87	26.75	92.74	26.44	116.30	38.06
Displacement thickness (δ^*)	4.27	3.35	4.67	3.74	4.69	3.33

further from the surface. Unlike the other turbulence models, the realizable k–ε model produces a definable gradient change where the velocity profile becomes quite blunt. The approximate location where the velocity profile exhibits this characteristic visually correlates well to the experimental and theoretical boundary layer thicknesses (i.e. $u \approx 99\% U_\infty$).

Tables III and IV detail the boundary layer parameters derived from the numerical data of each turbulence model, with comparison to the experimental and theoretical parameters at a free-stream velocity of 3 and 6 m/s, respectively. The superior performance of the realizable k–ε model is highlighted, accurately predicting the boundary layer thickness and displacement thickness to within 6.2 and 9.6%, respectively. The SST k–ω model predicts these parameters to within 27.7% and 16.2%, respectively, whilst the standard k–ε and standard k–ω turbulence models significantly over-predicted the boundary layer thickness (164.3 and 291%, respectively) and over-predict the displacement thickness (16.9 and 15.7%, respectively).

5.2.2. Suction surface boundary layer separation. To assess if each turbulence model correctly predicts suction surface boundary layer separation, analysis of the coefficient of skin friction on the surfaces of the hydrofoil was completed. For a two-dimensional steady-state flow, the full separation point (S) of the boundary layer can be approximately defined where the wall shear stress, hence the skin-friction coefficient, becomes zero [21].

Figures 7 and 8 illustrate the skin-friction coefficient distribution on the suction surface at the trailing edge for a free-stream velocity of 3 and 6 m/s, respectively. For 3 m/s, at approximately 96.5%C, all models predict a fluctuating increase in the skin-friction coefficient,

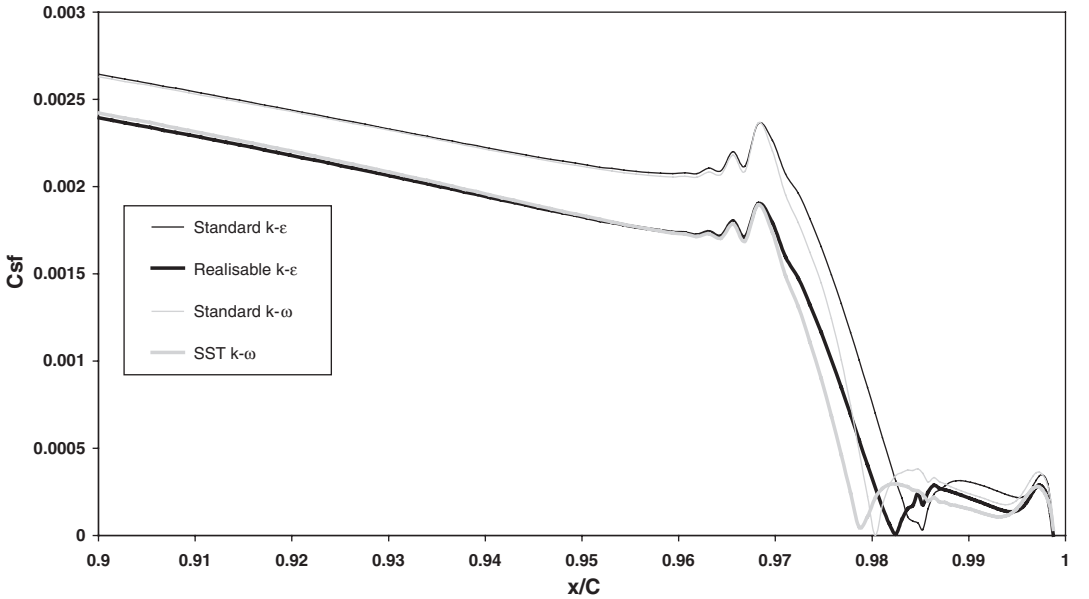

Figure 7. Turbulence model performance: skin-friction coefficient distribution on the suction surface at the trailing edge ($U_\infty = 3$ m/s).

peaking at a chordwise location of 96.8%C. Directly following the skin-friction coefficient peak is a steep decrease, reaching zero at a chordwise location of between 97.9 and 98.5%C (depending on the turbulence model). Beyond this chordwise location, a small secondary increase of the skin-friction coefficient occurs, followed by a gradual decrease to zero at the trailing edge (in Figures 7 and 8, the trailing edge terminates just prior to 100%C due to the fillet radius). The first chordwise location where the skin friction coefficient steeply decreases to zero is believed to be the location at which the boundary layer flow adjacent to the surface stagnates. This indicates that the fluid particles within the boundary layer flow directly adjacent to the surface are halted through the combined effects of the adverse pressure gradient and backflow from the recirculation zone. The second chordwise location where the skin-friction coefficient tends to zero again indicates flow stagnation and the partial reattachment of the boundary layer flow. The chordwise distance between these two points of boundary layer flow stagnation defines the length of the recirculation zone. With an increase in Reynolds number, the location at which the boundary layer flow fully separates moves rearwards (Figures 7 and 8); hence, a shorter recirculation zone is resulted, confirming the experimental observations of both Bourgoyne *et al.* [1] and Baubeau and Latorre [17].

Experimentally, boundary layer stagnation point was determined to occur between 97.8 and 98.6%C on the suction surface of the hydrofoil for 3 and 6 m/s [1]. The standard k–ε, realizable k–ε, standard k–ω and SST k–ω turbulence models predict full boundary layer separation at chordwise locations of 98.6, 98.4, 98.3 and 98.15%C, respectively. Compared with the experimental data, it seems that the location predicted by standard k–ω, SST k–ω and realizable k–ε turbulence models correlate better with the experimental measurement.

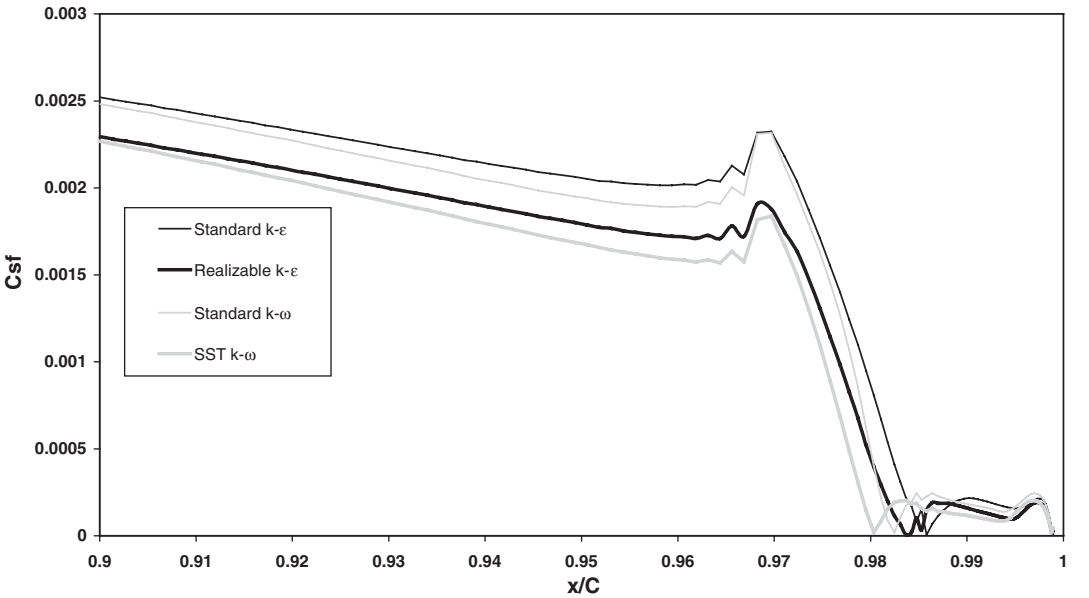

Figure 8. Turbulence model performance: skin-friction coefficient distribution on the suction surface at the trailing edge ($U_\infty = 6\,\mathrm{m/s}$).

5.2.3. Trailing edge and wake flow. The trailing edge and wake flow are shown in Figures 9–16. The normalized streamwise mean velocity profiles within the trailing edge region at chordwise location of 97.8.%C, the near wake 100 and 102%C for 3 m/s are demonstrated in Figures 9–11, respectively. At three locations, the standard k–ω, standard k–ε and the SST k–ω models under-predict the velocities above and below the trailing edge surfaces, possibly suggesting that the models are too diffusive, the realizable k–ε model, however, shows encouraging performance in resolving the important flow features, which may be attributed to a reasonable degree of damping possessed by the model. The computed size of the recirculation zone correlates very well with the experimental data. The realizable k–ε model also predicts the steep velocity gradient changes through the separating boundary layer flow. For the near wake region (102.8%C), a poorer velocity profile prediction is shown by each turbulence model compared with previous chordwise locations. All models over-predict the minimum velocity at the core of the wake and under-predict the transverse thickness of the wake region, showing poor correlation to the experimental data above the trailing edge.

The velocity profile for the far wake (150%C), a region of continuing turbulent kinetic energy dissipation, is illustrated in Figure 12. It can be seen that all models in the far wake predict a low velocity within the wake core. The 'downwash' effect of the flow over the hydrofoil is generally well predicted by each turbulence model, with the wake core being translated downwards with respect to its previous position in the near wake (Figure 11).

For analysis of the trailing edge and wake flow at a higher Reynolds number, Figures 13–16 illustrate the normalized streamwise mean velocity profiles 97.8, 100, 102.8 and 150%C, respectively, for a free-stream velocity of 6 m/s, corresponding to $Re = 1.657 \times 10^7$. The prediction

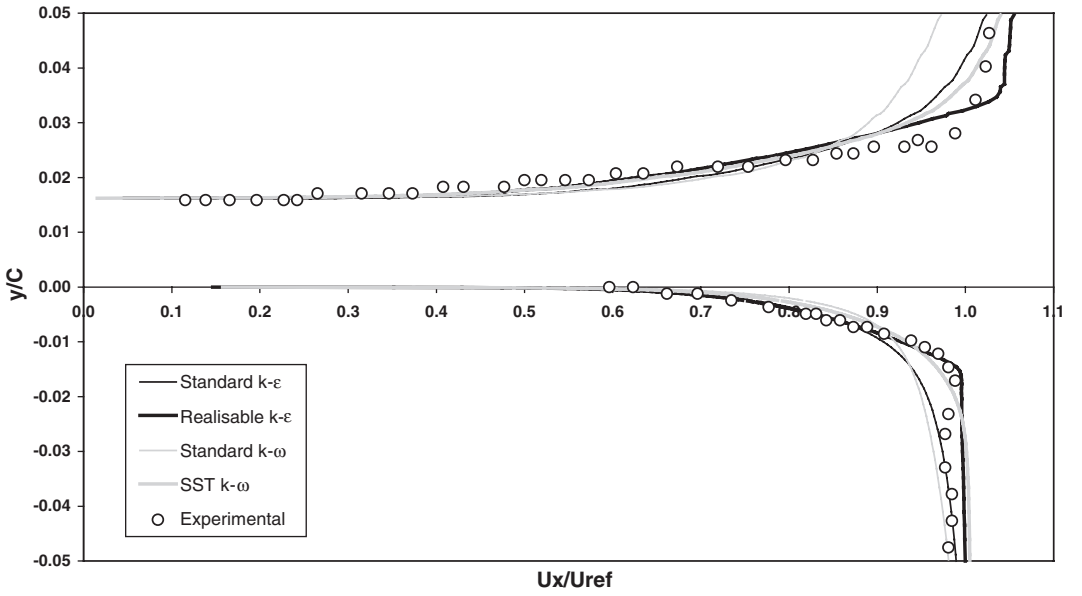

Figure 9. Turbulence model performance: normalized streamwise mean velocity profile at 97.8%C ($U_\infty = 3\,\mathrm{m/s}$).

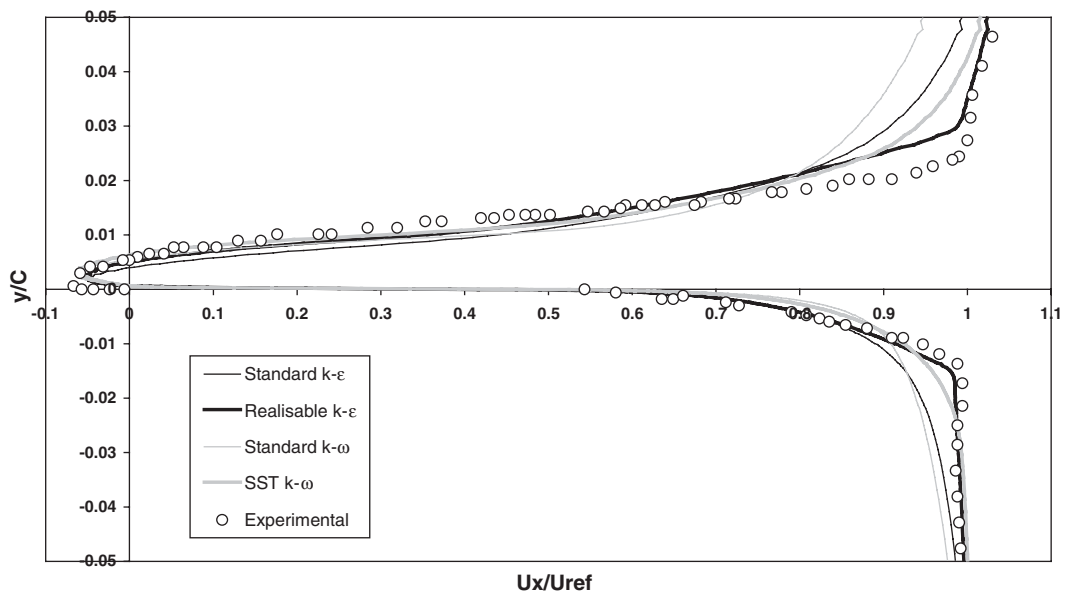

Figure 10. Turbulence model performance: normalized streamwise mean velocity profile at 100%C ($U_\infty = 3\,\mathrm{m/s}$).

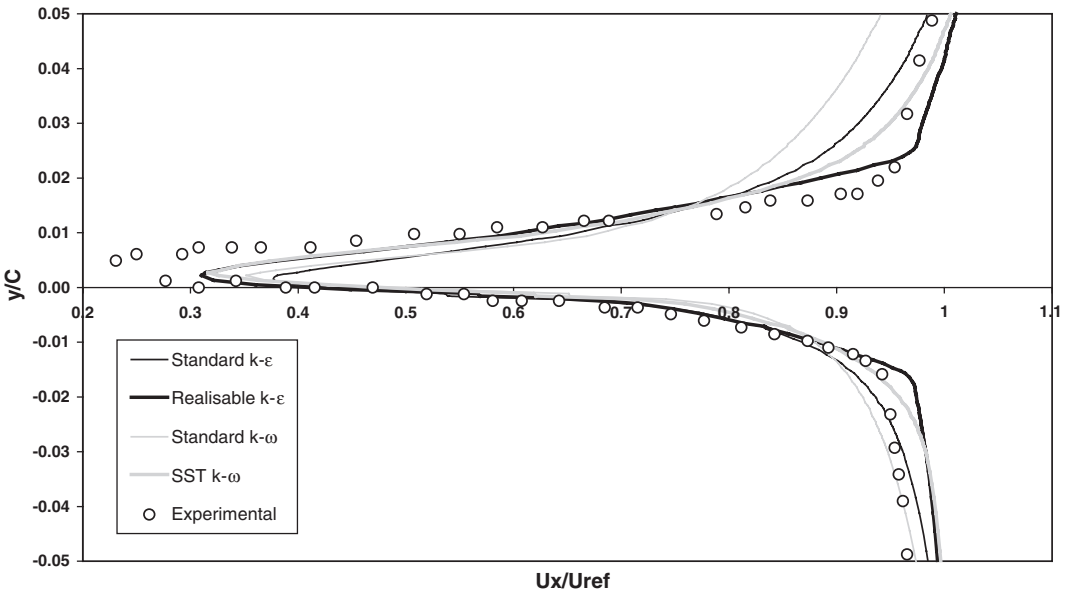

Figure 11. Turbulence model performance: normalized streamwise mean velocity profile at 102.8%C ($U_\infty = 3$ m/s).

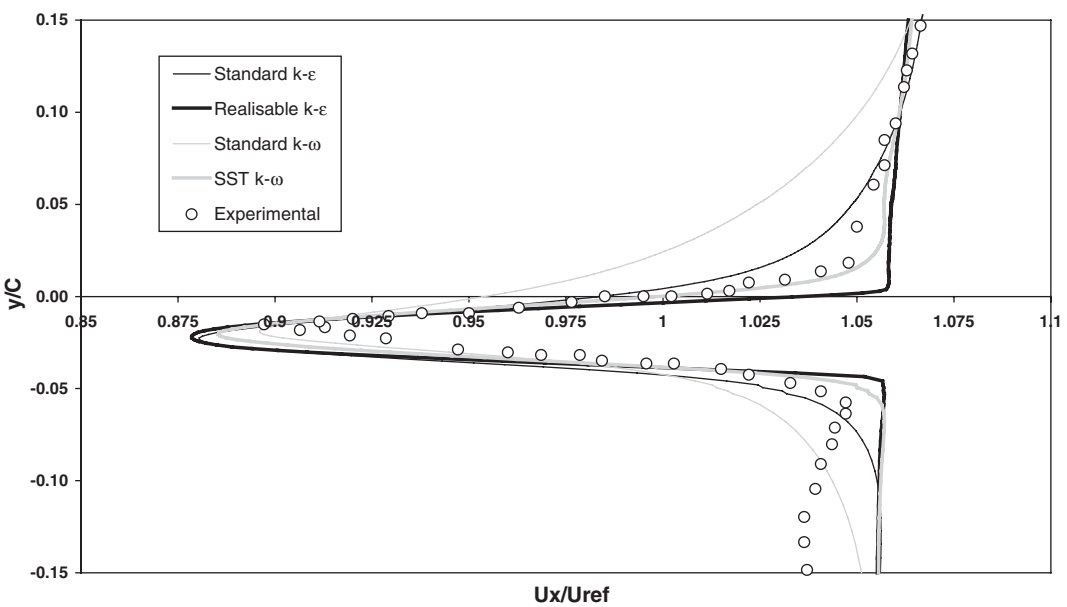

Figure 12. Turbulence model performance: normalized streamwise mean velocity profile at 150%C ($U_\infty = 3$ m/s).

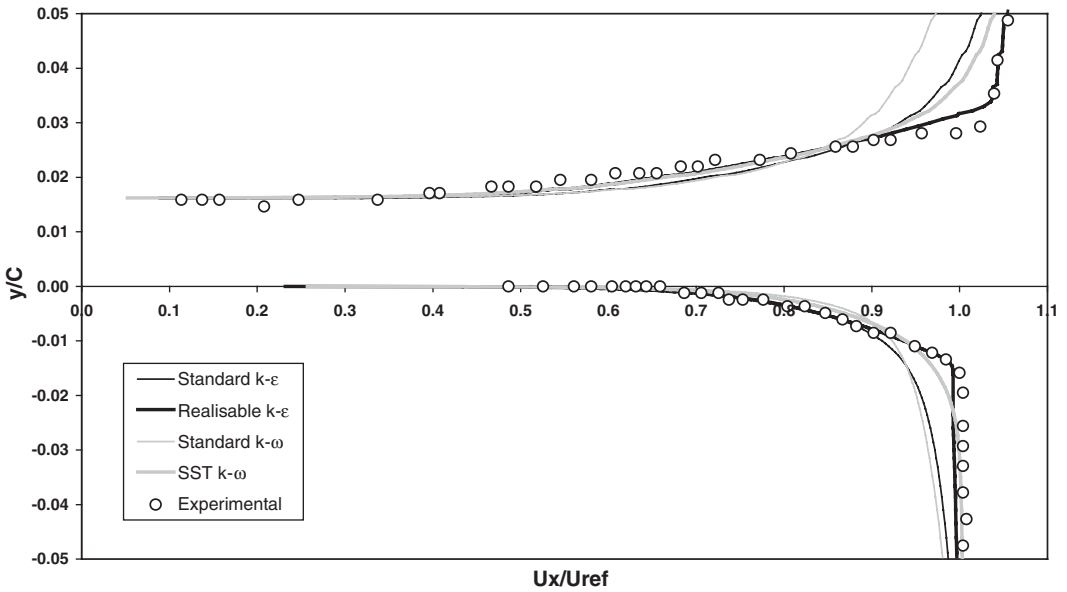

Figure 13. Turbulence model performance: normalized streamwise mean velocity profile at 97.8%C ($U_\infty = 6\,\mathrm{m/s}$).

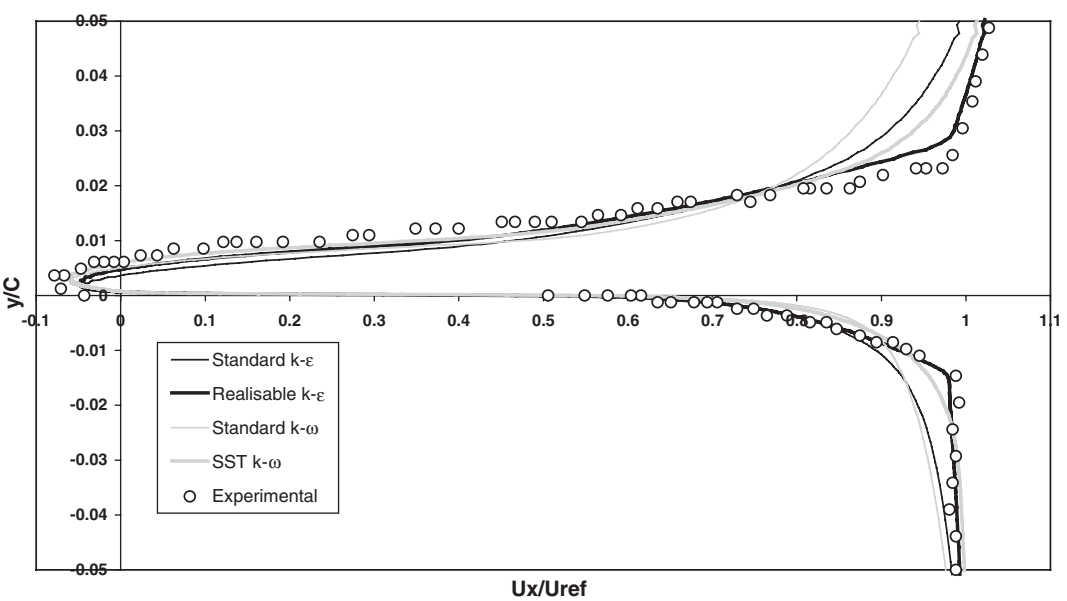

Figure 14. Turbulence model performance: normalized streamwise mean velocity profile at 100%C ($U_\infty = 6\,\mathrm{m/s}$).

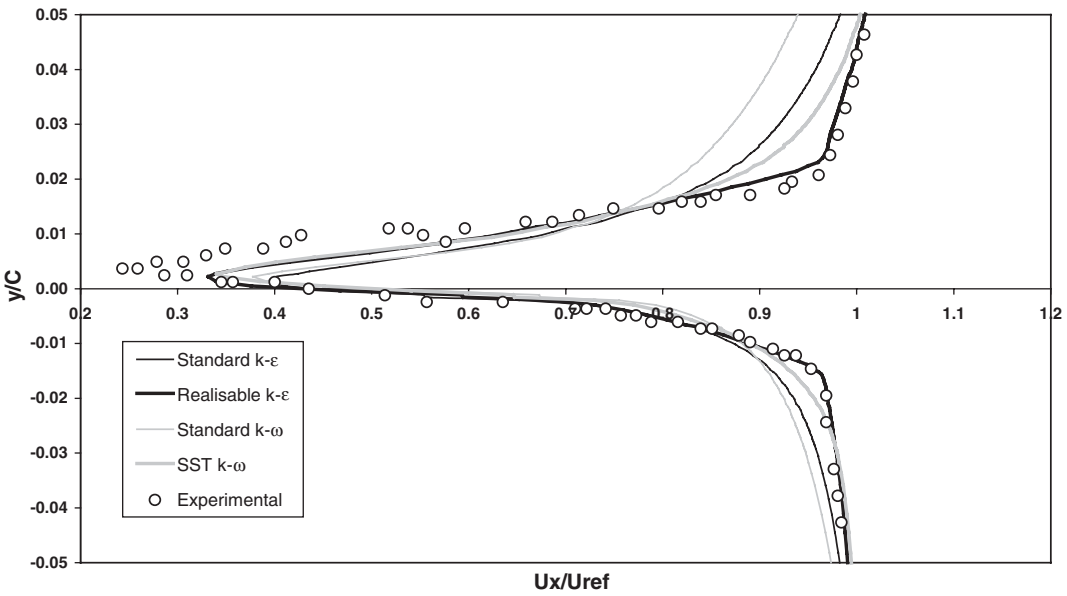

Figure 15. Turbulence model performance: normalized streamwise mean velocity profile at 102.8%C ($U_\infty = 6\,\mathrm{m/s}$).

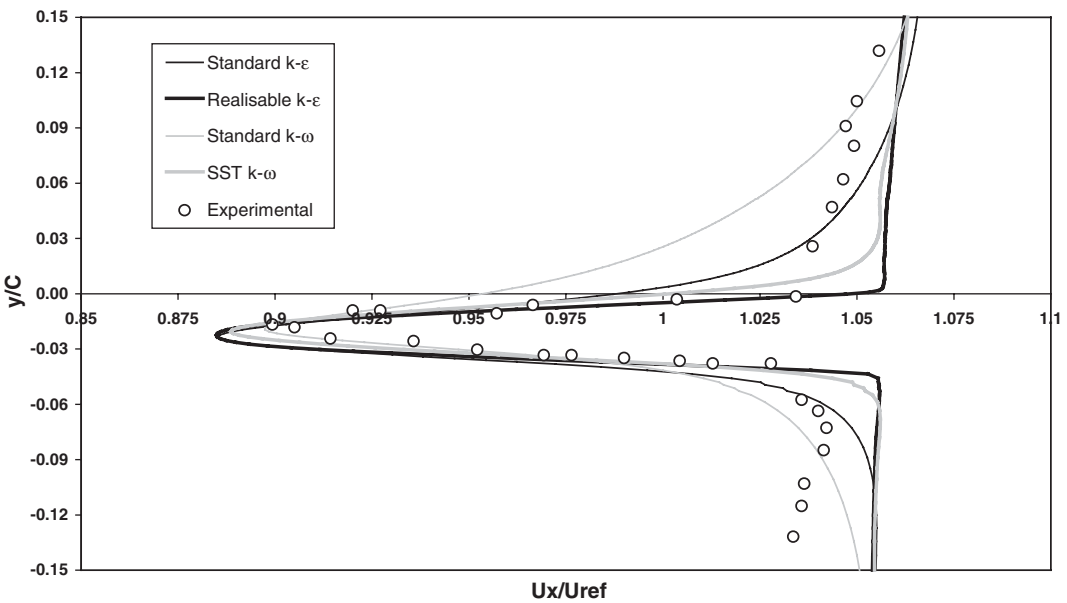

Figure 16. Turbulence model performance: normalized streamwise mean velocity profile at 150%C ($U_\infty = 6\,\mathrm{m/s}$).

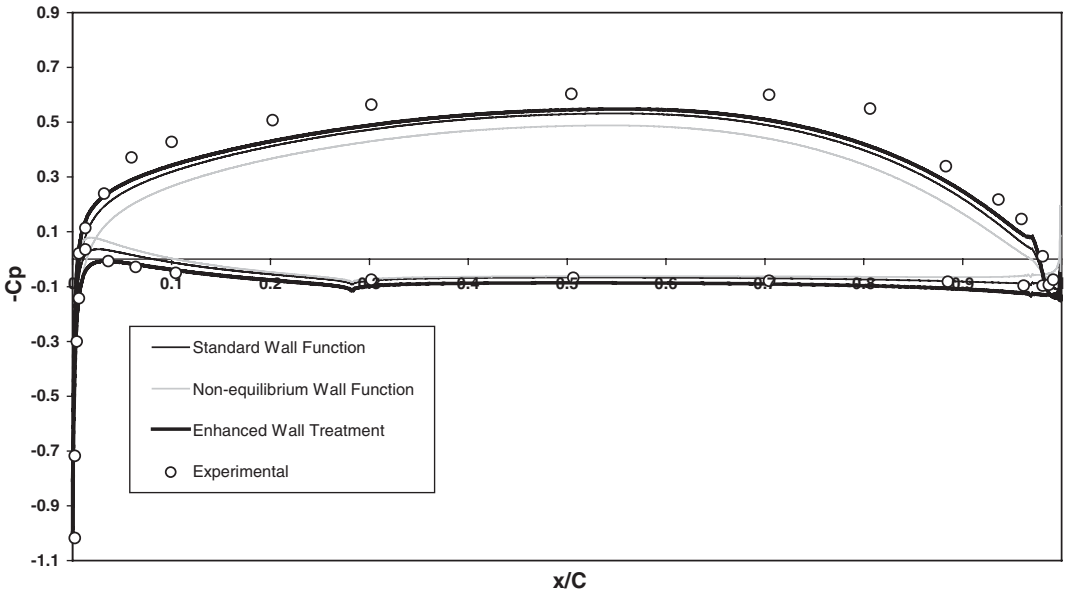

Figure 17. Wall treatment analysis: pressure coefficient (C_P) distribution at the surface of the hydrofoil ($U_\infty = 3$ m/s).

of each model for the higher Reynolds number flow is similar to the flow at 3 m/s. A slight improvement in the velocity profile prediction at the trailing edge and near wake is achieved.

5.3. Assessment of wall treatments

Results of the performance of the realizable k–ε turbulence model using the three wall treatments (the standard and non-equilibrium variants, and the enhanced wall treatment employing near-wall modelling techniques), at a free-stream velocity of 3 m/s ($Re = 8.284 \times 10^6$) are presented in Figures 17 and 18.

Figure 17 illustrates the coefficient of pressure distribution at the surface of the hydrofoil, predicted using the three different wall treatments. It is clear that the use of the wall treatments impacts the solution behaviour. As expected in flow scenarios involving strong adverse pressure gradients and boundary layer separation, the enhanced wall treatment produces the most accurate distribution. The use of the standard wall function produces a slightly less accurate prediction, yet performs generally well at the leading and trailing edges. However, the use of the non-equilibrium wall functions produces questionable results, particularly at the leading edge where the coefficient of pressure distributions on the suction and pressure surfaces cross each other.

Using the standard wall function, the coefficient of lift is largely under-predicted by 17.9%; however, this wall treatment produces a surprisingly accurate prediction of the coefficient of drag, only under-predicting the experimental value by 3.7%. Poorer predictions are shown using the non-equilibrium wall functions, under-predicting the coefficient of lift by 28.8%

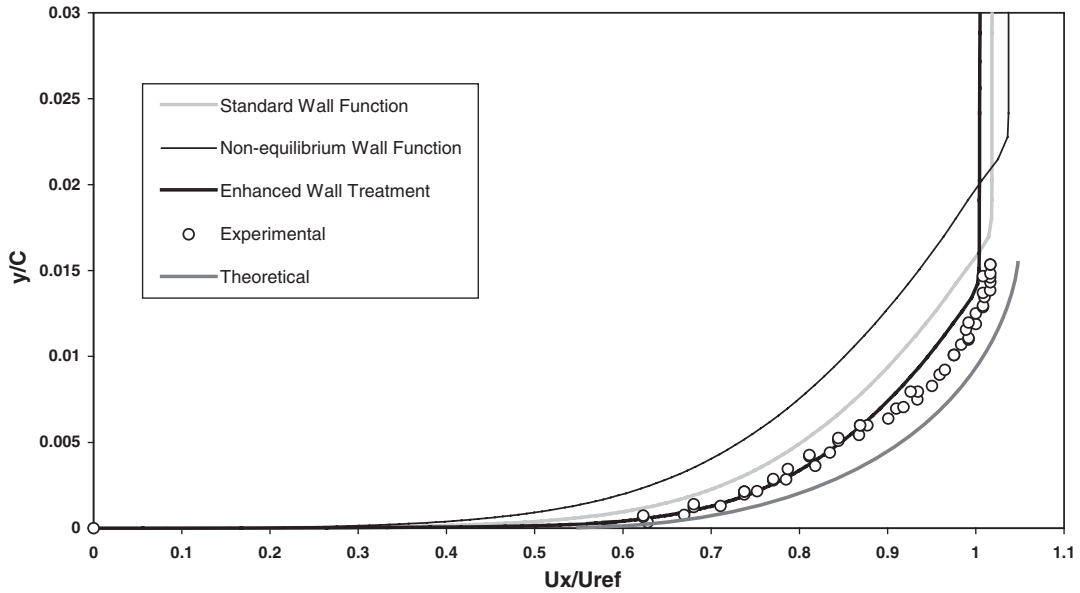

Figure 18. Wall treatment analysis: pressure surface boundary layer normalized mean velocity profile at 93%C ($U_\infty = 3$ m/s).

and over-predicting the coefficient of drag by 33.3%. The use of enhanced wall treatments produces generally accurate predictions of both the lift and drag coefficients to within 4.1 and 11.1%, respectively.

Figure 18 illustrates the numerical, experimental and theoretical pressure surface boundary layer velocity profiles at 93%C, at a free-stream velocity of 3m/s. As expected in the near wall region, the use of each wall treatment predicts a different boundary layer velocity profile. Again the use of enhanced wall treatment produces the most accurate velocity profile with comparison to the experimental data. The use of the standard wall function produces a boundary layer velocity profile with similar features to that produced by the enhanced wall treatment; however, a larger boundary layer thickness is predicted. Again, similar features are predicted using the non-equilibrium wall function, although, a much greater boundary layer thickness is predicted. The use of the enhanced wall treatment predicts the boundary layer thickness to within 6.2%, whereas the standard wall function and non-equilibrium wall function produce predictions to within 15.3 and 37.5%, respectively.

It should be noted that these results obtained using the three different wall treatments reaffirm the guidelines for the application of wall treatments to certain meshes and flow scenarios. With an average y^+ value of 2.31, the mesh used for this analysis is particularly fine (less than the desired value of 30) and is not classed as a 'wall function mesh'. Therefore, the validity of wall functions applied to this mesh is significantly degraded, producing poor numerical results. It is apparent that the standard wall function copes best in such an adverse application, whereas the non-equilibrium wall function performs rather poorly.

6. CONCLUDING REMARKS

Evaluation of the standard k–ε, realizable k–ε, standard k–ω and the SST k–ω RANS turbulence models against high-quality experimental data, has revealed that the realizable k–ε model shows vastly superior performance when applied in the steady-state analysis of hydrofoil turbulent boundary layer separation at high Reynolds numbers of 8.284×10^6 (3 m/s) and 1.657×10^7 (6 m/s).

The realizable k–ε turbulence model accurately predicts the pressure coefficient distribution at the surface of the hydrofoil, leading to good predictions in the overall pressure-derived lift and drag coefficients. Analysis of the turbulent boundary layer on the pressure surface of the hydrofoil at 93%C shows that the realizable k–ε model resolves the velocity profile, the boundary layer thickness and displacement thickness accurately. This model is also the sole model to correctly predict boundary layer thinning with an increase in Reynolds number.

Suction surface boundary layer separation from the trailing edge is also well predicted by the realizable k–ε turbulence model. The commencement location of boundary layer separation is accurately predicted, and this model correctly predicts that the full separation point of the turbulent boundary layer moves rearward with increasing Reynolds number, confirming experimental observations.

Even in the challenging separated trailing edge and near wake regions, the realizable k–ε model accurately predicts the normalized streamwise mean velocity profiles at four chordwise planar locations. The distinct performance advantage offered by the realizable k–ε model at these locations is the accurate prediction of the steep velocity gradient changes through the separating boundary layer flow, the recirculation size and the wake core in the near and far regions.

Compared with the respective results at Reynolds numbers of 8.284×10^6 (3 m/s) and 1.657×10^6 (6 m/s), the performance of the realizable k–ε model shows improvement with an increase in Reynolds number. Predictions of the hydrofoil's overall coefficients of lift and drag show improvement, the pressure surface boundary layer parameters are more accurately predicted, and considerable improvement is shown in the prediction of the normalized streamwise mean velocity profiles in the near and far wakes.

Furthermore, the analysis of three different wall treatments (standard and non-equilibrium wall functions, and enhanced wall treatment with near-wall modelling), shows that for flows involving severe adverse pressure gradients and boundary layer separation, the application of enhanced wall treatment may produce more accurate results. Confirming the guidance provided by [13], the application of wall functions to a considerably fine mesh significantly degrades their validity, producing poor numerical results. Therefore, the application of the realizable k–ε turbulence model with enhanced wall treatment to high-Reynolds number hydrodynamic flow scenarios, involving adverse pressure gradients and boundary layer separation, may provide researchers with more encouraging results.

ACKNOWLEDGEMENTS

This work was supported through a collaborative research agreement between the Maritime Platforms Division (MPD) of the Defence Science and Technology Organisation (DSTO) and the School of Aerospace, Mechanical and Manufacturing Engineering at RMIT University.

REFERENCES

1. Bourgoyne DA, Ceccio SL, Dowling DR, Jessup S, Park J, Brewer W, Pankajakshan R. Hydrofoil turbulent boundary layer separation at high Reynolds numbers. *23rd Symposium on Naval Hydrodynamics*, Val de Reuil, France, 2000.
2. Newman JN. *Marine Hydrodynamics*. Massachusetts Institute of Technology, MA, USA, 1978; p. 95.
3. Arabshahi A, Beddhu M, Briley W, Chen J, Gaither A, Janus J, Jiang M, Marcum D, McGinley J, Pankajakshan R, Remotigue M, Sheng C, Sreenivas K, Taylor L, Whitfield D. A perspective on naval hydrodynamic flow simulations. *22nd Symposium on Naval Hydrodynamics*, Washington, DC, USA, 2000; 920–932.
4. Speziale CG, Abid R, Anderson EC. Critical evaluation of two-equation models for near-wall turbulence. *AIAA Journal* 1992; **30**(2):324–331.
5. Wilcox DC. Reassessment of the scale-determining equation for advanced turbulence models. *AIAA Journal* 1988; **26**(11):1299–1310.
6. Wilcox DC. Multi-scale model of turbulent flows. *AIAA Journal* 1988; **26**:1311–1320.
7. Lien FS, Leshziner MA. Modelling 2D separation from a high-lift aerofoil with a non-linear eddy-viscosity model and second-moment closure. *Aeronautical Journal* 1995; 125–143.
8. Shin TH, Zhu J, Lumley JL. A realizable Reynolds stress algebraic equation model. *NASA* TM-105993, 1993.
9. Pajayakrit P, Kind RJ. Assessment and modification of two-equation turbulence models. *AIAA Journal* 2000; **38**(6):955–963.
10. Baldwin B, Lomax H. Thin-layer approximation and algebraic model for separated turbulent flows. *AIAA Paper* 1978; 78–257.
11. Dash SM, Beddini RA, Wolf DE, Sinha N. Viscous/inviscid analysis of curved sub or super-sonic wall jets. *AIAA Paper* 1983; 83–1697.
12. Kim WJ, Kim DH, Van SH. Computational study on turbulent flows around modern tanker hull forms. *International Journal for Numerical Methods in Fluids* 2002; **38**:377–406.
13. Fluent Inc. *FLUENT 6.0 User's Guide*. NH: USA, 2001.
14. Bourgoyne DA, Ceccio SL, Dowling DR, Hamel JM, Judge CQ. Lifting surface flow, pressure and vibration at high Reynolds-number. *ASME International Conference and Exposition*, New York, USA, 2001a.
15. Bourgoyne DA, Ceccio SL, Dowling DR, Hamel JM, Judge CQ. *Hydrofoil Testing at High Reynolds Number*. CP, Department of Mechanical Engineering, University of Michigan, Michigan, USA, 2001b.
16. Gorski J, Nguyen, P. Navier–Stokes analysis of turbulent boundary layer wake for two-dimensional lifting bodies. *Eighteenth Symposium on Naval Hydrodynamics*, Ann Abor, USA, 1991; 633–643.
17. Baubeau R, Latorre, R. Numerical study of the boundary layer transition for two-dimensional NACA 16-012 and 4412 hydrofoil sections. *Journal of Ship Research* 1986; **30**(1):43–50.
18. Baubeau R, Latorre R. Numerical study of wall influence on boundary layer transition for two-dimensional NACA 16-012 and 4412 hydrofoil sections. *Journal of Ship Research* 1990; **34**(1):38–47.
19. Baubeau R, Latorre R. Numerical study of hydrofoil boundary layers. *Ocean Engineering* 1995; **22**(1):87–95.
20. Internet Reference www.dt.navy.mil/div/capabilities/facilities/5004.html (Accessed: 4th of August, 2002).
21. Gersten K, Schlichting H. *Boundary Layer Theory* (8th edn). Springer: Berlin, Germany.

